Explicit nested-grid prediction of convective-scale motions in a skillful global model

Lucas M. Harris[1], Matthew Morin[1,2], Shannon Rees[1,2], Linjiong Zhou[1,3], and William F. Stern[1,2]

[1]NOAA/Geophysical Fluid Dynamics Laboratory
[2]University Corporation for Atmospheric Research
[3]Atmospheric and Oceanic Sciences Program, Princeton University

Key Points:

- A global-to-regional refined atmosphere model is presented for simultaneous, skillful global and convective-scale predictions.
- Year-round and springtime forecasts show skill equal to or better compared to operational global and regional models.
- Models based on the Finite-Volume Cubed-Sphere Dynamical Core show great promise for unifying global and regional prediction systems.

Corresponding author: Lucas Harris, `lucas.harris@noaa.gov`

Abstract

Global convective-scale models are currently too expensive to be operationally useful, but limited-area convective-scale models are only useful for a few days' lead time. We present a new global model able to be locally refined so as to explicitly-resolve convection over a small area of the earth. This model, fvGFS, couples the GFDL Finite-Volume Cubed-Sphere Dynamical core (FV^3) to the Global Forecast System (GFS) physics and initial conditions, augmented with a six-category microphysics and a modified planetary boundary layer scheme. The goal is three-fold: skillful global predictions, explicit simulation of mesoscale- and storm-scale circulations, and useful multiple-day prediction of convective-scale events, all in the same model. Here we examine the characteristics of fvGFS on a 3-km continental United States domain nested within a 13-km global model. Retrospective forecasts from all seasons are evaluated, with a focus on severe continental convection. The nested fvGFS still has good hemispheric skill comparable to or better than the operational GFS; meanwhile, convective-scale phenomena, especially supercell thunderstorms and squall lines, are explicitly represented over the refined region. In particular, fvGFS has excellent representation of fine-scale updraft helicity fields, an important proxy for severe weather forecasting. Precipitation skill is found to be superior to operational global models and competitive with operational regional models; the 3-km domain also greatly improves upon 2-m temperature and humidity biases in the global model. We discuss further development of fvGFS and the prospects of a unified global-to-regional prediction system.

1 Introduction

Advances in numerical modeling and computer capacity in the last two decades has allowed great strides in improved prediction at global and convection-permitting or convection-allowing scales [*Bauer et al.*, 2015; *Clark et al.*, 2016, and references therein]. Recently, unified global-to-regional systems [*Walters et al.*, 2017] have been discussed as a way to combine the ability of convective-scale regional models to predict individual thunderstorms and the medium-range and longer prediction capabilities made possible by a global model, to allow extended-range explicit prediction of convective storms and to reduce the dependence upon convective parameterization. Global modeling brings the benefits of longer-range prediction and relieves the need for driving boundary conditions from a global model, but also raises many challenges. Global modeling is more expensive, since the domain size is fixed, and modeling of the general circulation is challenging owing to the great diversity in world-wide phenomena and geographical features, all of which need to be correctly simulated or parameterized for a successful forecast. Regional models have the luxury of optimizing for the particular region being simulated: In particular, the characteristics of tropical and mid-latitude convection are greatly different [*Emanuel*, 1989], with major implications for the microphysical and convective parameterizations. A global model must maintain stability when confronted with the steep topography of the Himalayas, the Andes, and at the edges of polar ice sheets, and must also represent the powerful stratospheric winds with speeds a significant fraction of the speed of sound, violating the assumptions commonly made in regional models. A global model capable of effective simulation of convective-scale features must address all of these concerns; the need for skillful prediction only magnifies these challenges.

Our research group at GFDL has developed a new global weather forecast model, the Finite-Volume Global Forecast System (fvGFS), which replaces the spectral dynamical core used in the operational Global Forecast System (GFS) with the GFDL Finite-Volume Cubed-Sphere Dynamical core, FV^3 [or FV3: *Putman and Lin*, 2007], in addition to other improvements to the GFS physical parameterization suite. A series of companion papers will describe this model in more detail and the many applications being developed with this model, including hydrostatic-scale prediction, tropical cyclone prediction, and global cloud-resolving modeling. This paper will demonstrate the utility of the variable-resolution capabilities of FV^3, especially grid nesting, to permit the explicit simulation of convective motions over the Contiguous United States (CONUS) in a global model; a second paper will describe results from a complimentary grid-refinement strategy using a single variable-resolution grid.

We will show objectively that the global skill of the base global model is maintained when the grid is locally refined. We will also show that fvGFS can simulate realistic mesoscale and storm-scale features, including severe convection, and can predict such features both on the 0–36 hour timescales for which convective-scale models are currently used and also on medium-range timescales of several days. The nested fvGFS described here serves as an initial prototype of a unified global-to-regional model capable of skillful global-scale prediction and effective convective-scale prediction—all in the same modeling system, in the same forecast. Further development will entail introduction of modern physics packages, especially revisions to the microphysics and planetary boundary layer scheme, and improvements to the initialization, including radar and satellite data assimilation.

The manuscript is organized as follows. Section 2 describes the fvGFS model and its configuration for the simulations described in the rest of the manuscript. Section 3 describes the quantitative evaluation of the model, both global and regional forecast skill and biases, and the aggregate characteristics of the simulations. Section 4 describes individual nested forecasts to demonstrate the qualitative characteristics useful for prediction, especially for severe convective events. Section 5 summarizes the paper and discusses the prospects for a unified modeling system.

2 Model description and configuration

The fvGFS forecast model is built around the nonhydrostatic FV^3 dynamical core, the most recent version of FV^3 and the Finite Volume (FV) core used for many years in NOAA, NASA, NCAR, and elsewhere for global chemical [*Bey et al.*, 2001] and aerosol [*Chin et al.*, 2000] transport modeling, climate modeling [*Delworth et al.*, 2006; *Zhao et al.*, 2009; *Neale et al.*, 2010; *Donner et al.*, 2011; *Zhao et al.*, 2016; *Bogenschutz et al.*, 2017], seasonal prediction [*Chen and Lin*, 2011, 2013; *Murakami et al.*, 2015], real-time weather and air-quality forecasting [*Suarez et al.*, 2008], the Reanalyses MERRA and MERRA-2 [*Rienecker et al.*, 2011; *Gelaro et al.*, 2017], global mesoscale and cloud-resolving modeling [*Shen et al.*, 2006; *Putman and Suarez*, 2011; *Lin et al.*, 2017], simulation of Martian climate [*Greybush et al.*, 2012], and radiative-convective equilibrium modeling [*Jeevanjee*, 2017]. FV^3 solves the fully-compressible Euler equations using the forward-in-time scheme and Lagrangian vertical coordinate of *Lin* [2004], the scalar advection scheme of *Lin and Rood* [1996] based on the piecewise-parabolic method, the Lagrangian dynamics of *Lin and Rood* [1997], and the finite-volume pressure gradient force of *Lin* [1997]. Fast vertically-propagating sound- and gravity-wave processes are handled by a traditional semi-implicit solver. The horizontal discretization is on the gnomonic equiangular cubed-sphere grid [*Putman and Lin*, 2007] capable of local refinement by two-way grid nesting [*Harris and Lin*, 2013, 2014] and grid stretching [*Harris et al.*, 2016] through the *Schmidt* [1977] transformation.

The GFS physics used for the simulations described here use the most recent scale-aware Simplified Arakawa-Schubert [SA-SAS, *Han et al.*, 2017] shallow and deep convection schemes; the GFS planetary boundary layer scheme [*Han and Pan*, 2011]; and the Rapid-Radiative Transfer Model [RRTM, *Clough et al.*, 2005]. The simple microphysics scheme of *Zhao and Carr* [1997] and cloud fraction scheme of *Xu and Randall* [1996] is replaced by the GFDL six-category microphysics *Chen and Lin* [2013] augmented with the ability to perform fast phase changes and latent heating at a faster timescale than the rest of the physical parameterizations (to be described in a forthcoming manuscript by L. Zhou et al). The Noah land surface model [*Ek et al.*, 2003], upgraded to use high-resolution land surface data [*Wei et al.*, 2017], provides land-surface interactions.

The nested-grid configuration of fvGFS used here uses a global cubed-sphere grid with 768 by 768 grid cells (c768) on each of the six sides of the cube, rotated and stretched by a factor of 1.5 to reach a grid-cell-width of roughly 9 km over the CONUS. A factor-of-three two-way nest is then placed over the CONUS, yielding 3-km grid-cell width (Figure 1). The model uses 63 Lagrangian vertical levels on both grids, each using the GFS hybrid-pressure levels as the reference vertical coordinate; the first model layer is centered between 15 and 25 m above the surface, depending on the atmospheric conditions, with 14 layers below 1.5 km and 19 below 3 km. On the coarse global grid, the tracer advection, vertical remapping, and physical parameterizations use a 90-s timestep, with an acoustic-mode timestep of approximately 12.5 s. On the nested grid, the same 90-s physics timestep is used, but the tracer advection, vertical remapping, and fast microphysical processes use a 22.5-s timestep, and the acoustic-mode timestep is 4.5 s. This choice of timesteps is stable for all of the simulations described in this paper, while remaining efficient and also allowing us to perform the fast latent heating processes at a frequency appropriate for convective scales. Interactions between the nested and coarse grids (boundary conditions and two-way updating) occur every 90 s. The radiation scheme is updated hourly.

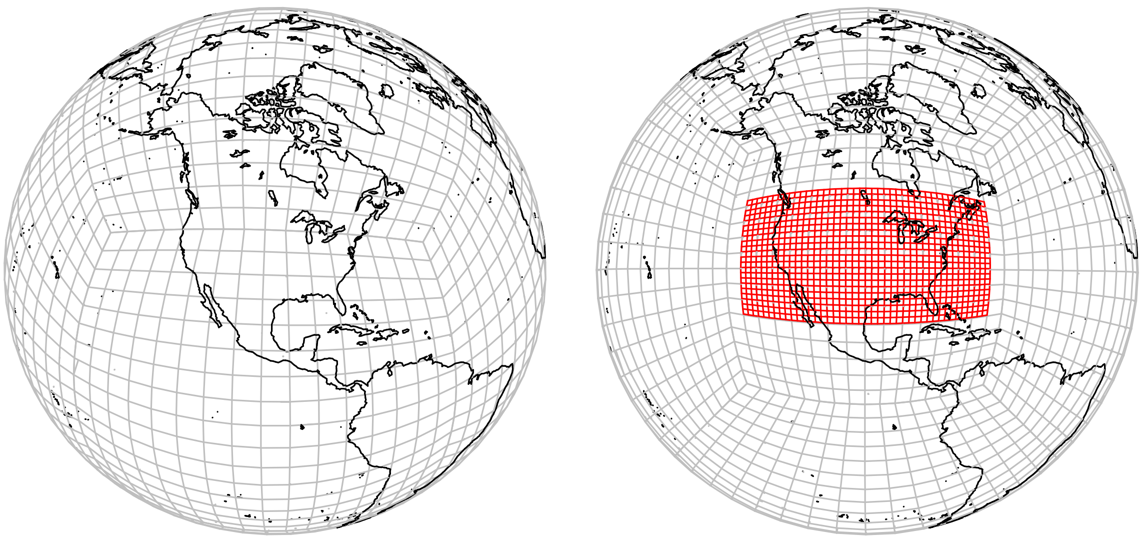

Figure 1. Structure of uniform global grid (left) and global stretched cubed-sphere (gray) and CONUS nested (red) grids (right).

Some modification of the GFS physics on the nested grid is necessary for best results at convective scales. We disable the convective parameterization (both shallow and deep) on the nested grid, unless noted otherwise. To address issues with the GFS PBL scheme on convective scales [*Hong et al.*, 2006], we constrain the local vertical mixing in the boundary layer by reducing the parameterized turbulent diffusivity by half, and disable the diffusion in the inversion layer. Further improvements to the boundary layer scheme are being developed.

The model is currently cold-started from operational GFS analyses, of about 13 km nominal resolution; no data assimilation or other initialization techniques are used.

We present model forecasts for two time periods. One is a 74-case set of "hindcasts" initialized at 00Z every five days from 16 January 2015 to 15 January 2016. This set of forecasts include a very broad range of synoptic-scale regimes across all seasons, and permits a very robust evaluation of forecast skill and model robustness. We have found that hemispheric forecast skill can vary significantly on a month-to-month basis, and skill in a 30- or even 60-day period may be unrepresentative of the year-round skill. The simulations are 7 days long during this time period, and use two configurations, one with ("SA-SAS nested fvGFS") and one without ("nested (noconv) fvGFS") SA-SAS enabled on the nested grid; otherwise the two configurations are identical. (Unless otherwise stated all nested model results refer to nested noconv fvGFS.)

The second time period covers the 77 forecasts run daily at 00Z from 01 April to 16 June 2017 for the Hazardous Weather Testbed (HWT) Spring Forecast Experiment (henceforth simply "Spring Experiment" period), which imposes a requirement to have forecasts finished, post-processed, and delivered to HWT by roughly 7am CDT each day. Only the nested noconv configuration was run for this period. This time period included a number of significant severe-weather outbreaks, which are useful cases to show the capabilities of fvGFS. All nested fvGFS simulations during this period are integrated to 120 hours.

3 Forecast skill and aggregate simulation characteristics

The coarsest-grain metric for forecast skill is that of the hemisphere-wide 500-hPa height. A good 500-hPa skill does not necessarily mean that a given model will give better forecasts of impactful weather, but poor 500-hPa skill indicates degraded forecasts, especially at longer lead times. Plots of Northern and Southern Hemisphere root-mean square error (RMSE; K) and anomaly correlation coefficient [ACC; *Murphy and Epstein*, 1989] for the 2015 all-season hindcasts are shown in Figure 2, for the two sets of nested hindcasts. For reference, they are compared to both the operational GFS as well as the GFDL real-time 13-km uniform-resolution fvGFS (henceforth referred to as the 13-km fvGFS), which has been aggressively optimized for large-scale skill. Table S1 summarizes the configurations of all of the models mentioned in this paper. For this time period, the 13-km fvGFS has RMSE and ACC which are statistically-significantly improved over the operational GFS (lower RMSE and higher ACC), especially after day 5. The two nested hindcast suites, which have not been as optimized for global simulation, show a slightly poorer skill but still better than the GFS after the first two days. This reduction in skill is likely due to the mismatch in resolution between the convective scales over the CONUS needing to spin up from the coarser GFS analyses; overall, there is a minor degradation of the hemispheric 500-hPa skill in a two-way nested run. The runs during 2017 Spring Experiment period (Figure S1) have a more modest improvement over the operational GFS, owing to improvements in the operational model and month-to-month forecast skill variability.

Of more direct importance to human activity are surface measures of temperature and humidity. RMSE and bias for 2-m temperature (T2m) and 2-m dew point temperature (DPT2m) over the eastern and western US are shown in Figure 3 for the 2015 hindcasts; Figures 4 and 5 show the spatial distribution of the biases, for a 24-hour forecast and averaged over the entire forecast period, respectively. The CONUS T2m errors are significantly lower in the nested fvGFS than in the operational GFS, while the 13-km fvGFS shows smaller but still significant improvements over the GFS. The nested fvGFS shows a significant reduction in cold and dry biases compared to the operational GFS; the 13-km fvGFS shows a smaller improvement to these biases. In the western US the nested fvGFS shows a significant reduction in cold biases, especially over the intermountain region and Pacific Northwest, although a nighttime warm bias has emerged in the Great Plains region. The errors and biases in nested fvGFS were nearly identical in the SA-SAS nested and nested noconv configurations, demonstrating the scale-awareness of SA-SAS.

The most important and most difficult to forecast impact is precipitation. Figure 6 shows the skill scores, measured by equitable threat score [ETS; *Wang*, 2014], fractions skill score [FSS; *Roberts and Lean*, 2008], and bias score compared to observed precipitation from the Stage IV multi-sensor quantitative precipitation estimate [*Lin and Mitchell*, 2005; *Lin*, 2011] for both sets of 2015 year-round hindcasts; here, we present both ETS and FSS to show that our results are not specific to a certain measure of precipitation skill. As expected, we find that both ETS and FSS are highest at about 12–24 hours after initialization and for the lightest precipitation rates, and then decreases steadily for longer lead times and higher rates. ETS and

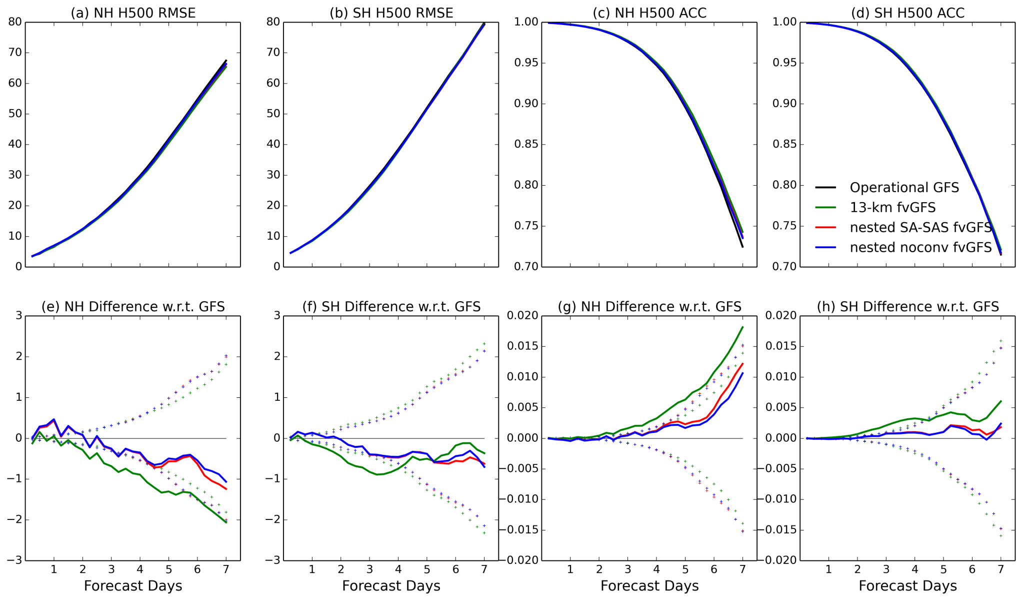

Figure 2. Hemisphere-wide 500-hPa height skill for 2015 year-round hindcasts. Top row: (a) northern-hemisphere (NH: 20–80 N latitude) and (b) southern-hemisphere (SH: 80–20 S latitude) root-mean square error, lower is better; (c) northern-hemisphere and (d) southern-hemisphere anomaly correlation coefficient, higher is better. Bottom row: (e–h) as in (a–d) but relative to the contemporary operational GFS; dotted lines represent 95% confidence interval for the differences from GFS.

FSS are highest for the period 18Z-00Z each day, and is slightly higher in the SA-SAS nested fvGFS. For both versions of the nested fvGFS, the bias scores are close to 1 (optimal) for light and moderate precipitation, with a low bias for heavy precipitation rates (over 25 mm/6hr; Figure 4f); in all cases the nested fvGFS has smaller biases than the 13-km models. The SA-SAS nested fvGFS shows modestly reduced low bias for heavy precipitation but also more light precipitation; the skill scores are nearly the same. The nested fvGFS substantially improves upon the biases of the 13-km fvGFS for all precipitation thresholds but has lower skill, especially in FSS and for lighter precipitation rates. All of the fvGFS versions show a substantial improvement over the operational GFS on the wet bias over the western US (Figure 7), although the improvement of the nested model over the 13-km fvGFS is more minor except over the southwestern US.

We can also compare fvGFS to the operational 3-km nest of the North American Model (NAM; see overview at `http://www.emc.ncep.noaa.gov/mmb/mmbpll/misc/NAM_2017.pdf`) during the Spring Experiment period (2015 NAM output was no longer available as of this writing). The skill and biases of the nested fvGFS are largely comparable to those of the NAM (Figure 8); in fact, both fvGFS versions have slightly better skill for light precipitation rates, and the NAM has a high bias in heavy precipitation while nested fvGFS has a low bias. The nested fvGFS has similar biases to the NAM in the eastern two-thirds of the US, and reduced high biases in the Western US, as well as less noise in regions of complex terrain (Figure 9). We can also compare the temperature and dew point errors to those of the NAM during the Spring Experiment period (Figures S2 and S3); at 24 hours the temperature errors over the Eastern US are comparable to those of the nested fvGFS, but the NAM has lower warm and dry biases over the central plains.

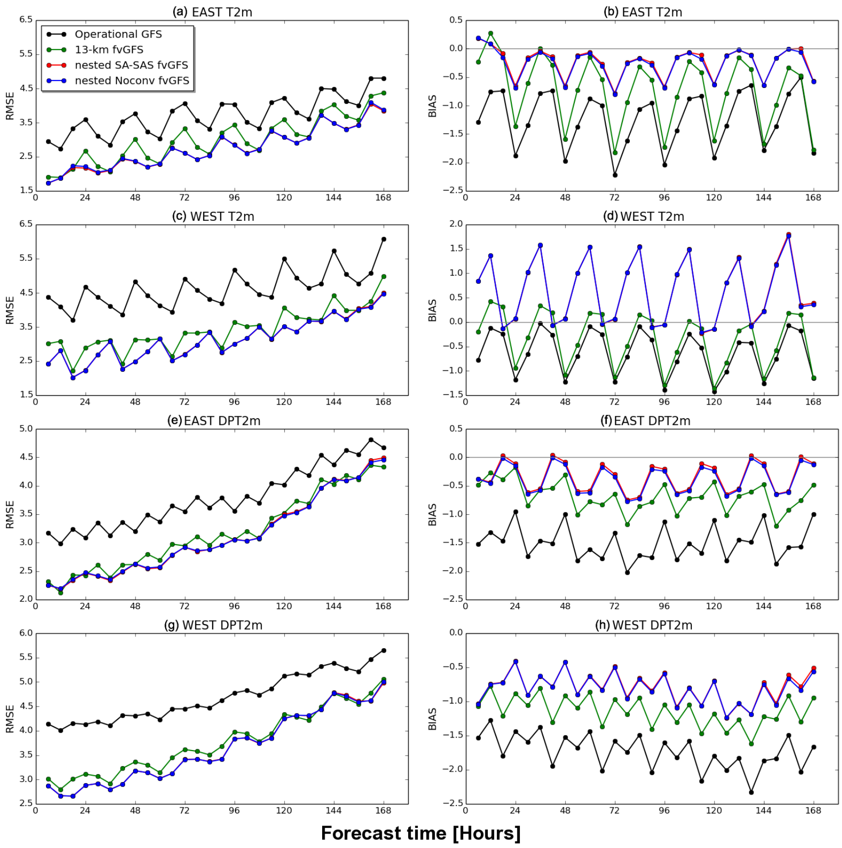

Figure 3. RMSE (K; a,c,e,g) and bias (K; b,d,f,h) for Eastern US 2-m temperature (a,b), Western US 2-m temperature (c,d), Eastern US 2-m dew point temperature (e,f), and Western US 2-m dew point temperature (g,h) during the 2015 year-round hindcasts. The definitions of east and west regions are given at `http://www.emc.ncep.noaa.gov/mmb/research/nearsfc/nearsfc.verf.html` .

A broader indication of the behavior of individual systems can be seen in the time-longitude plots in Figure 10, depicting a meridionally-averaged plot of precipitation from each day's nested fvGFS forecasts at different lead times during an active period in May 2017. Both rapidly-moving thunderstorm outbreaks and the more slowly-propagating but longer-lived synoptic-scale systems are apparent, and compare very well with Stage IV in timing, positioning, and strength. The consistency between the forecasts at different lead times is remarkable, and numerous outbreaks are correctly predicted even 84–108 hours in advance of the event. When compared against the 13-km fvGFS (Figure S4), it is apparent that although both models are able to capture the broad areas of precipitation, the nested fvGFS has a much better representation of small propagating and more rapidly-propagating systems, which appear as streaks with a shallower angle in Figure 10. This difference between the parameterized and explicit convection is most noticeable for the event on 20–21 May, which even four days in advance appears as a coherent, rapidly-propagating feature in the nested fvGFS.

We can average a number of forecasts to determine whether fvGFS captures the diurnal cycle of precipitation. Figure 11a,b show the meridionally-averaged precipitation averaged over each forecast during May 2017 as a function of forecast hour for the 13-km (a) and the nested (b) fvGFS, compared to the observed diurnal cycle (Figure 11c) during the same month. The broad-scale features, particularly the eastward propagation of systems, the evening (03z to 06z) maximum in precipitation over the Great Plains (100W to 90W), and the morning-to-afternoon precipitation over the Eastern US, are all captured by the nested model; the 13-km

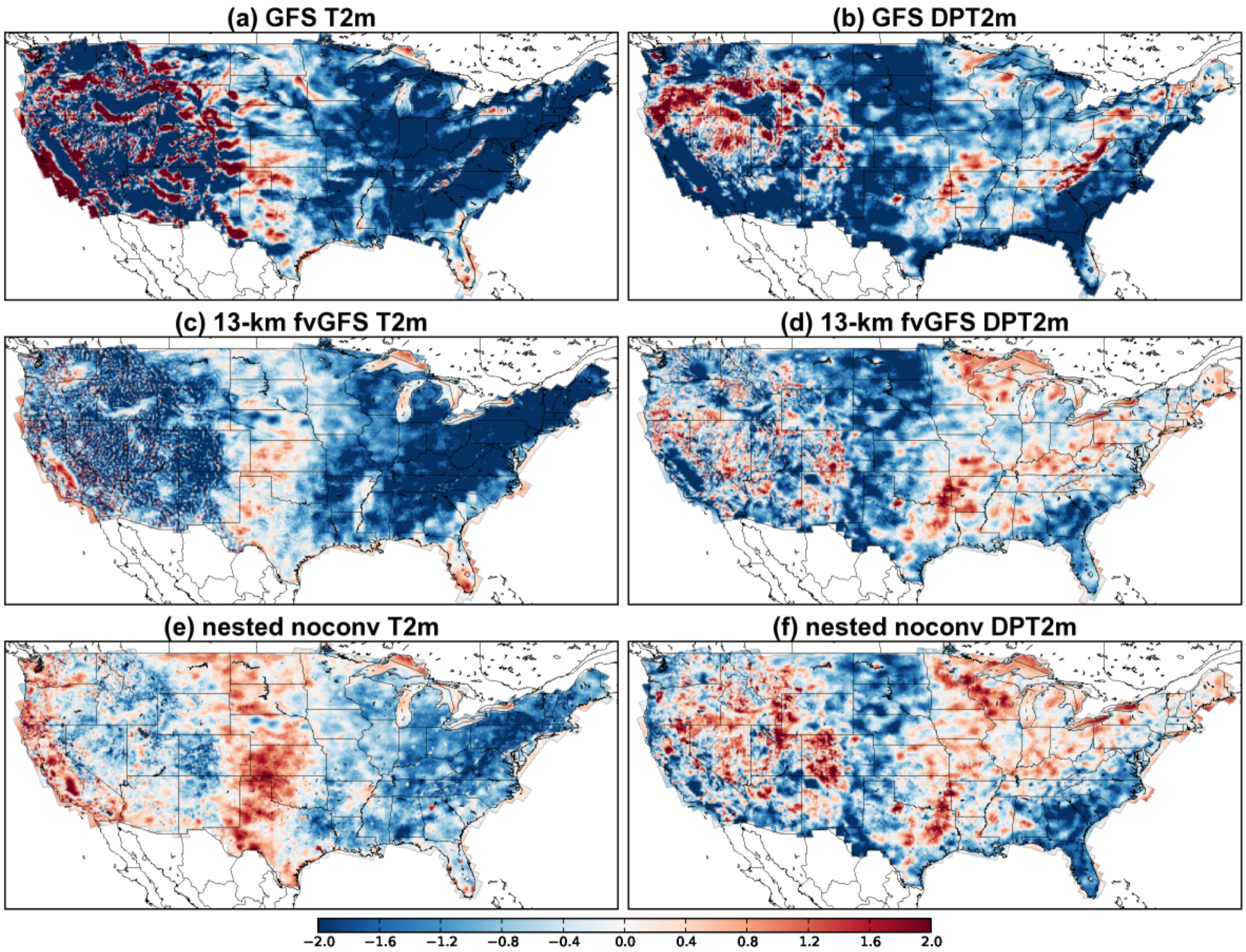

Figure 4. Biases of 2-m temperature (T2m, K; a,c,e) and 2-m dew point temperature (DPT2m, K; b,d,f) at 24 hours after initialization during the 2015 year-round hindcasts for the operational GFS (a,b), 13-km fvGFS (c,d), and nested noconv fvGFS (e,f).

model's parameterized convection shows some sign of eastward propagation, albeit less coherent and typically weaker. The amounts of precipitation are largely faithfully reproduced by the model, except for a low bias between 85W and 75W. The amplitude of the simulated diurnal cycle in the nested model is less than observed over the western half of the region (90 to 110 west longitude; Figure 11d) and greater than observed in the eastern half (70 to 90 west longitude; Figure 11e), although the 13-km model shows very little diurnal amplitude in the eastern half.

4 Mesoscale and storm-scale model characteristics of nested fvGFS

In the previous section the objective forecast skill of the nested fvGFS has been demonstrated. We now show specific examples of the characteristics of predicted weather systems in the 3-km nested fvGFS. We will focus on warm-season severe weather since the 3-km runs were specifically designed for the Spring Experiment. Unless otherwise noted, all references to the model are to nested (noconv) fvGFS

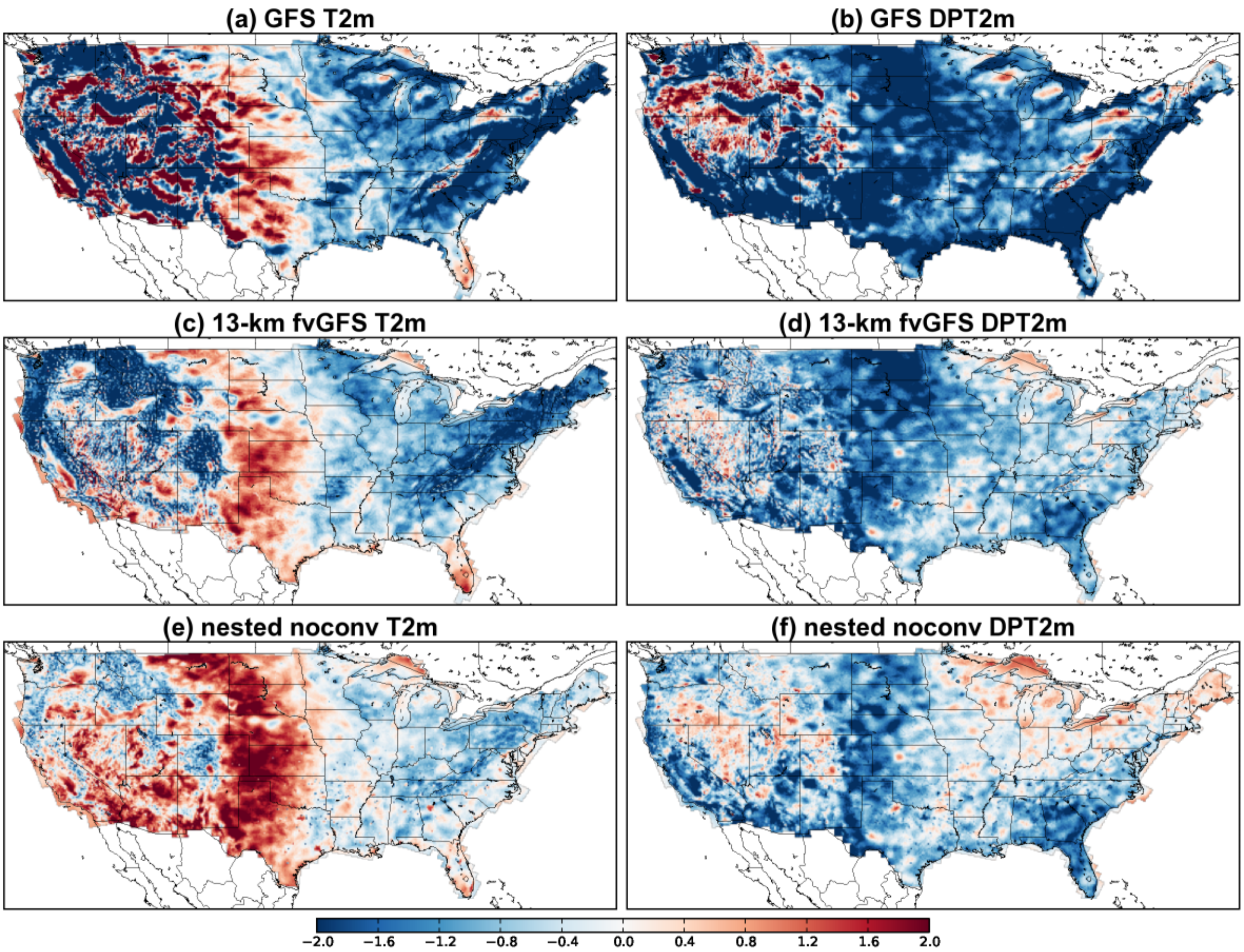

Figure 5. As in Figure 4, but for the entire 0–5 day forecast period.

4.1 Multi-scale predictability: 30 April–1 May 17 squall line

A frontal squall line is an example of an event which is strongly forced by synoptic-scale disturbances but also embeds many small-scale cells, which can alter the propagation of its neighboring storms and can feed back onto the mesoscale organization of the line. Figure 12 depicts an event on 30 April–1 May 2017 in which a long-lived cold-frontal squall line is propagating eastward from west of the Mississippi river through the Gulf Coast states. The fvGFS forecast correctly predicts the positioning of the main squall line at 18Z and 00Z (Figure 12a,b) while correctly depicting the long line of individual convective cells at the front of the squall line, stretching from Tennessee down to the Gulf coast, with a substantial trailing stratiform region of lighter reflectivities, and correctly predicts the decay of the northern part of the line by 00Z. The development of a post-frontal squall line by 06Z is also predicted, although the model generates it much earlier than observed and strengthens it much more slowly, with intense reflectivities not seen until after 06Z.

Since the model is cold-started from a coarse-resolution GFS analysis, a spin-up period is necessary before storm-scale features are fully developed. However it is interesting to examine the behavior of the model as it equilibrates. Figure 13 shows the same 1 May event but for initialization 00Z on 1 May. In the first hour after initialization (Figure 13a), the structure of the squall line is very similar to what we might expect from a hydrostatic-scale model, although some small-scale convection in unstable areas is already beginning to appear in Mis-

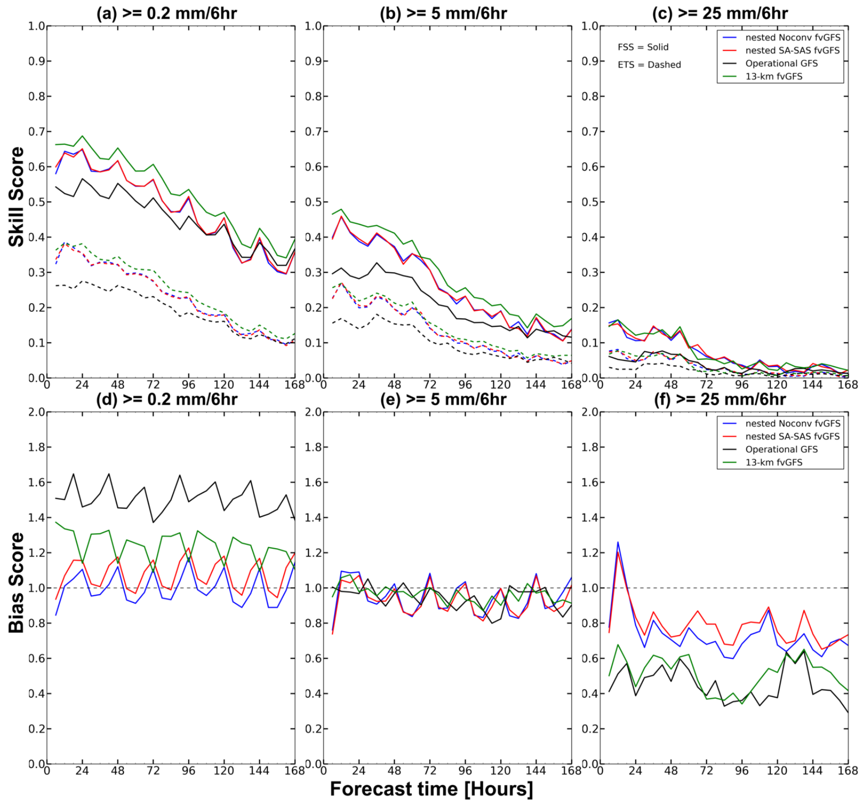

Figure 6. Comparison of Skill scores (a–c; ETS dashed, FSS solid), and Bias scores (d–f) between the two nested fvGFS configurations and the operational GFS for the 2015 year-round hindcasts, for precipitation rates greater than or equal to 0.2 (a,d), 5.0 (b,e) and 25.0 (c,f) mm/6 hr. All models are re-gridded to 4-km resolution to match the Stage IV verification and a 12-km neighborhood is employed for ETS and FSS.

sissippi and in Georgia. The GFS analysis contains no precipitating hydrometeors and thus would be devoid of radar echoes; so all of the precipitating hydrometeors are produced by fvGFS during its equilibration. Later times (Figure 13b–d) show more small-scale detail as well as better organization of mesoscale features, such as the multiple contiguous bands of moderately-strong echoes, lines of discrete cells, and the formation of stratiform regions. Fortuitously, the placement and structure of some of these features is very accurate, especially at 09Z (Figure 13c).

A more rigorous examination of model spin-up can be made by computing the kinetic energy spectrum [cf. *Koshyk et al.*, 1999] of the nested-grid region. Figure 14 shows the spectrum of 250 mb kinetic energy computed using the two-dimensional discrete fourier transform of *Denis et al.* [2002], which at these resolutions should roughly follow a -5/3 slope [*Nastrom and Gage*, 1985]. At one hour after initialization (blue) the larger scales (> 100 km) present in the analysis are represented in the model, but there is much less activity at smaller scales than we would expect from a -5/3 spectrum. The conspicuous exception is near the $4\Delta x$ cutoff of representable scales by the model, at which some small-scale motions (presumably convection, as in Figure 12a) has already started. By three hours after initialization (green), the intermediate (20–100 km) scales have largely been filled-in, as have the marginally-resolved scales ($4\Delta x$–$6\Delta x$), with a sharp cutoff of the poorly-resolved scales below $4\Delta x$; by six hours (red), the spectrum now closely resembles the average (heavy black line) over the rest of the five-day forecast. A similar spin-up of Hurricane Harvey (2017) within a few hours has also been seen in a different 3-km nested configuration (A. Hazelton, personal communication). Although this rapid spin-up may not occur for all regimes, particularly more weakly-forced warm-

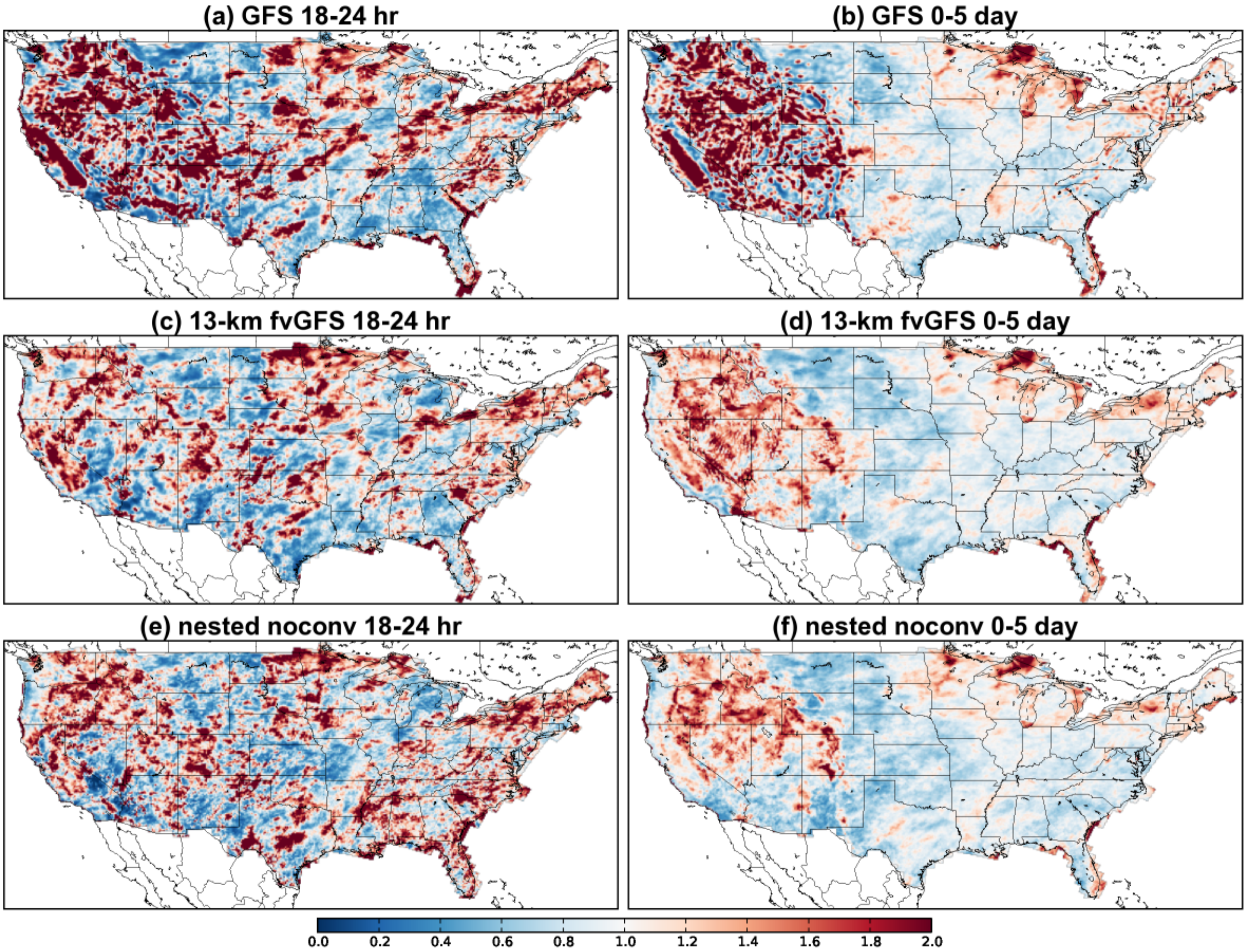

Figure 7. As in Figure Figure 4, but showing ratio of modeled to observed precipitation (fractional bias; 1 implies no bias) during the 2015 year-round hindcast period.

season events, this result does show the possibility for very rapid equilibration in fvGFS, useful for both data assimilation and nowcast applications.

There is still substantial variability in the magnitude and the shape of the spectrum even during this five-day forecast, especially at the smallest resolved scales; further experiments (Figure 14, right) representing all seasons show that there can be strong regime-dependent shifts in the spectral shape, spectral slope, and even total energy of the nested region, which are exacerbated if the region on which the analysis is performed is reduced. This is the opposite of our experience with globally-uniform fvGFS simulations [*Lin et al.*, 2017] which typically have very robust global kinetic energy spectra across runs, even at uniform global 3-km resolution. These results suggest that caution is warranted in interpreting spectra from limited-area models for limited numbers of events or over a small domain.

4.2 Storm-scale structure: 18 May 17 Central Plains supercells and squall line

A compelling advantage of convective-scale models is that they are able to explicitly simulate the convective mode, providing useful information as to the likelihood of particular hazards. While the predictability of any one cell is very low, this sort of model can be used to predict the region in which severe thunderstorms may occur. However, while 3-km grid-spacing

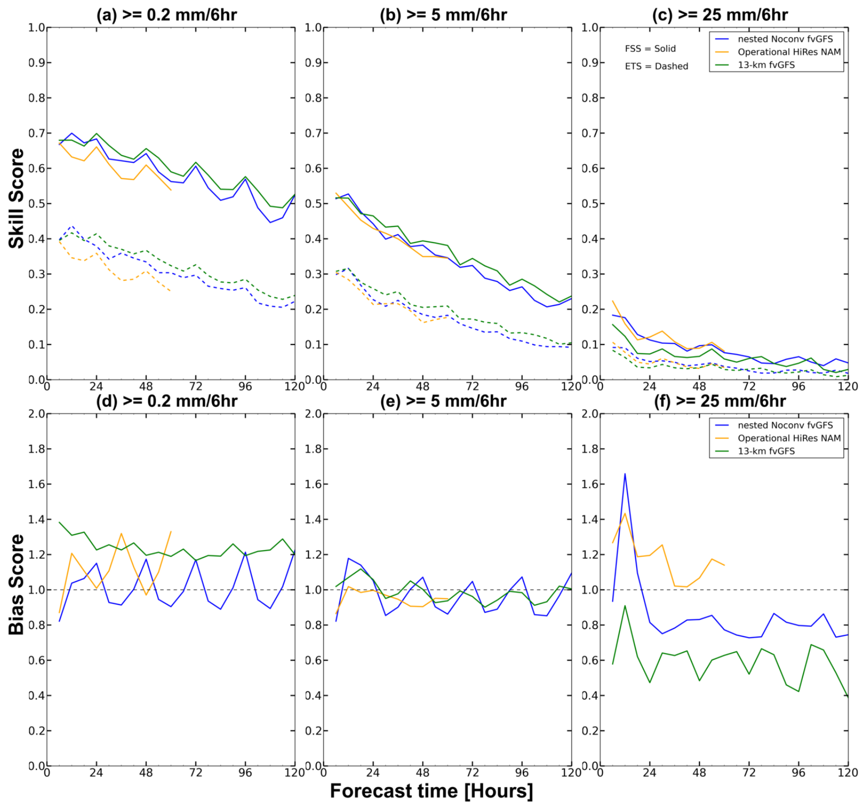

Figure 8. As in Figure 6 but for the 2017 Spring Experiment period and comparing the 13-km and the nested fvGFS to the operational NAM.

is able to resolve rotating updrafts, it cannot resolve tornadoes or microbursts, requiring the use of proxy diagnostics such as updraft helicity to determine the possibility of hazardous events.

Figure 15 shows the predicted and observed composite reflectivities for a supercell outbreak in western Oklahoma into southern Kansas on the evening of 18 May 2017. The nested fvGFS correctly predicts the initiation of discrete cells along the Oklahoma-Texas border at 20Z, and correctly predicts the evolution into an elongated squall line after 00Z with a cyclonic turning over Nebraska; the line does propagate more quickly than observed, with too-early initiation over Texas.

Figure 16 shows a close-up of storm-scale structure in the Oklahoma supercells shortly after initiation. Several individual cells are visible from the composite (Figure 16a) and base (Figure 16b) reflectivity fields, with broad stratiform regions of moderate (20–40 dBz) and visible convective cores, although the base reflectivities of the cores are weaker than observed. (A forthcoming manuscript will describe a similar set of nested fvGFS simulations using the microphysical scheme of *Thompson et al.* [2008], in which the convective cores are much stronger but the stratiform regions less extensive). Both the cores and the stratiform regions are visible in the column-integrated condensate (Figure 16c), indicating large amounts of water and ice near the core and smaller amounts into the stratiform regions.

The coherent structures in the hourly-maximum of composite reflectivity (Figure 16d) indicates that intense, marginally-resolved moving or propagating systems are being correctly represented in fvGFS. To see this, we examine hourly-maximum updraft helicity (UH), the vertical integral of the product of vertical velocity and vertical vorticity (Figure 17a–d), and the hourly-maximum column-maximum updraft (Figure 17e–h). Numerous coherent, elongated

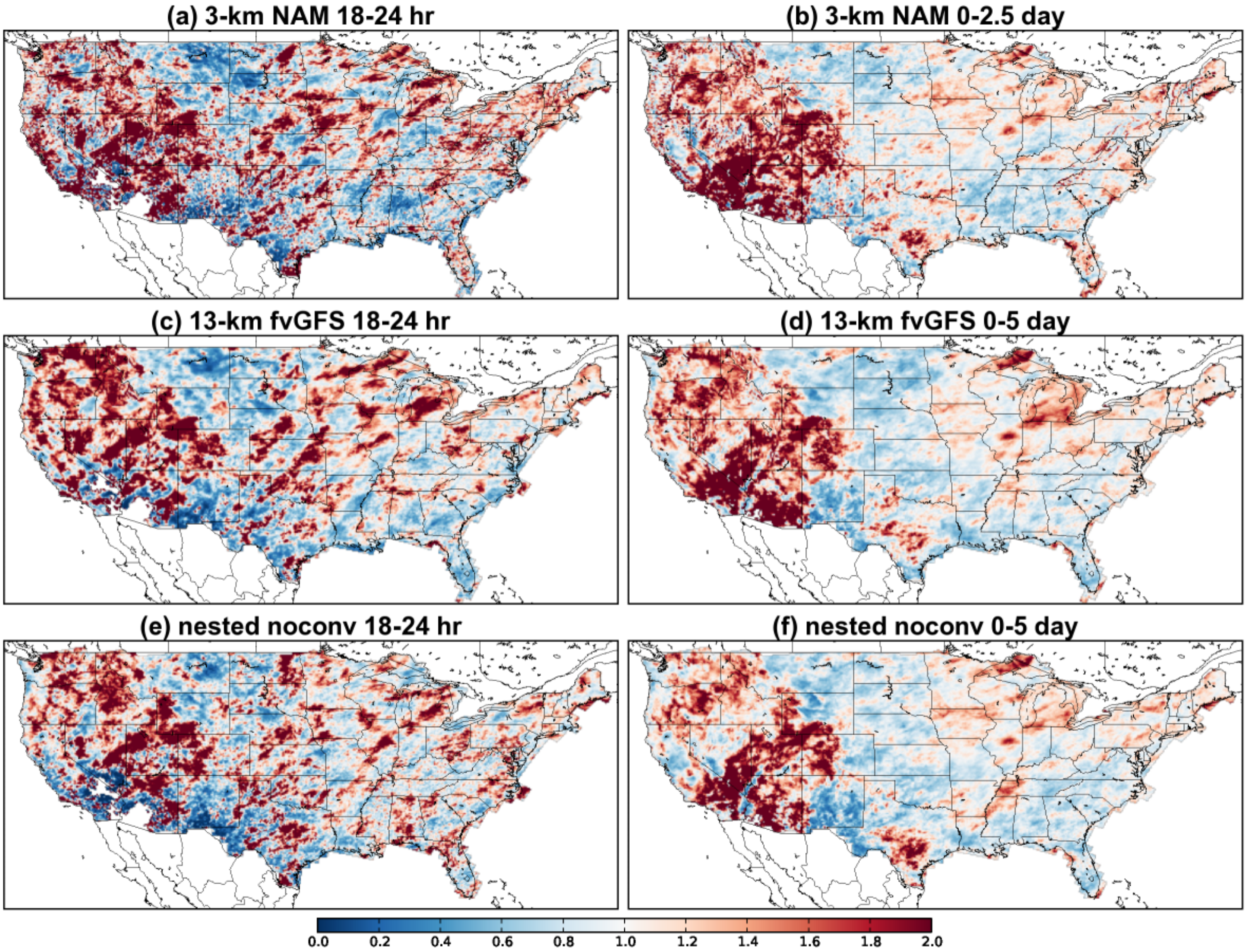

Figure 9. As in Figure 7 but for the Spring Experiment period, and comparing to the operational NAM nest, for which totals are shown for the 60 hour duration of the NAM forecast.

streaks are visible in the UH field, with some features only one or two grid cells wide. These features are maintained for an extended period as they move with their parent storm; they are well-represented rotating updrafts in the model, and not numerical noise, despite their very small size. The same finely-detailed features are visible in the hourly- and column-maximum updrafts, indicating that both vorticity and vertical velocity are well-represented in fvGFS, even near the grid scale.

FV^3 was designed to accurately represent and advect the (vertical) vorticity and any of its products with a cell-average scalar as if it was itself a scalar, as described for shallow-water potential vorticity (mass times vorticity) by *Lin and Rood* [1997]; in particular fine-scale features and sharp gradients are very well preserved. Updraft helicity is the product of vorticity and vertical velocity, both cell-mean quantities in FV^3, and so fvGFS is able to represent coherent, long-lived features in this field even near the grid scale.

4.3 Multi-day prediction: 27–28 May 17 "Triple Derecho"

Derechos are intrinsically driven by intense discretely-propagating thunderstorm cells and are very difficult to represent with the parameterized convection of current medium-range prediction models. We present forecasts of the "triple derecho" of 27-28 May 2017 (Figure 18)

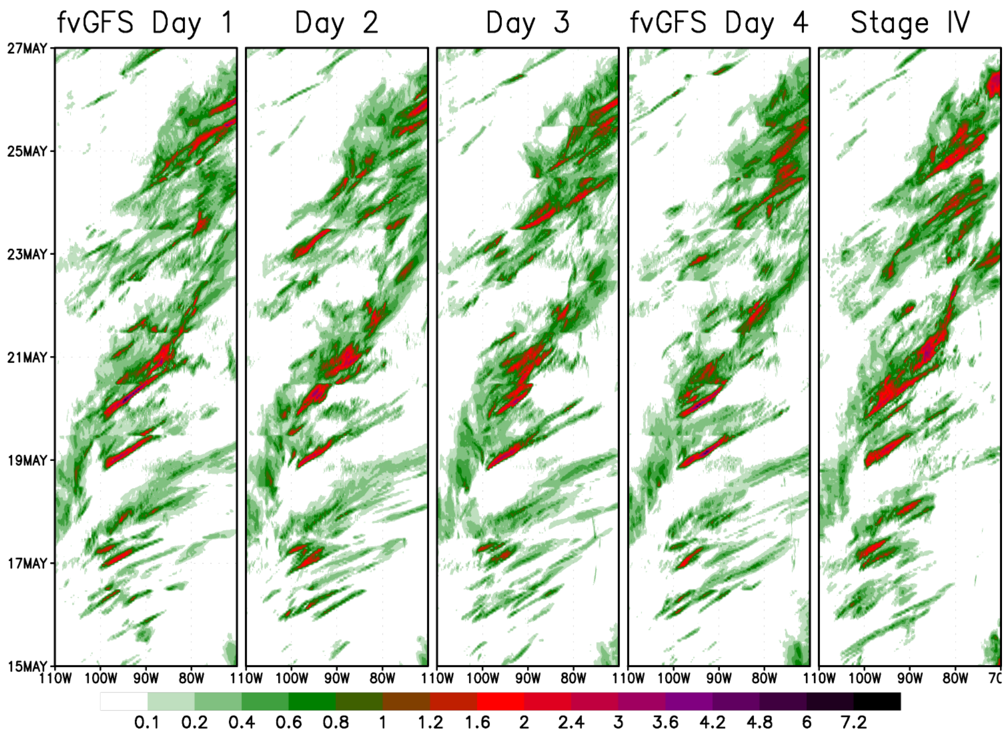

Figure 10. Time-longitude plots of hourly-accumulated precipitation (mm) in daily nested fvGFS forecasts, for different lead times of 12–36 hours (day 1), 36–60 hours (day 2), 60–84 hours (day 3), and 84–108 hours (day 4), compared to Stage IV multi-sensor observed precipitation. The results are averaged from 30 to 50 latitude, for the period of 15 to 27 May 2017.

as first identified by the Storm Prediction Center (SPC), in which three individual events in the Ohio valley were observed, each fulfilling the *Corfidi et al.* [2016] definition of derecho. The forecast initialized at 00Z that day (Figure 19) clearly shows three extensive, rapidly-propagating bowing features; the first moving through Kentucky and Tennessee, the second moving from Missouri through Tennessee into Alabama and Georgia, and the third moving through Arkansas, all broadly in agreement with the timing and positioning of the observed events. The maximum values of the 2–5 km updraft helicity during this event (Figure 20a) shows the tracks of the successive systems through this region, although the axes of maximum helicity values are displaced slightly southward of the observed storm reports.

This derecho event was predictable several days in advance, longer than the longest-lead forecast of operational US convection-allowing models. Predictions 48, 72, and 96 hours in advance (Figure 21) all show multiple bow echo signatures reminiscent of derechos in the Ohio and lower Mississippi Valleys, although the precise timing varies and there is a tendency towards too much activity in eastern Texas. The forecast initialized on 24 May (Figure 20b) again shows large regions of high updraft helicities organized along a couple of main tracks, although oriented more from the southwest to the northeast than the later forecast (Figure 20a) and with less activity in Missouri.

The environmental conditions to predict this derecho were predictable in both the 3-km nested and 13-km fvGFS. Figure 22 shows that a synoptic-scale environment favorable for bow echoes and derechos was predicted up to five days in advance of the event, with strong unidirectional shear and high convective available potential energy in Missouri and Arkansas and eastward through the Ohio Valley. That the environment was well-predicted is substantiated by the predictions from the real-time 13-km fvGFS shown in Figure 23: a squall line is cor-

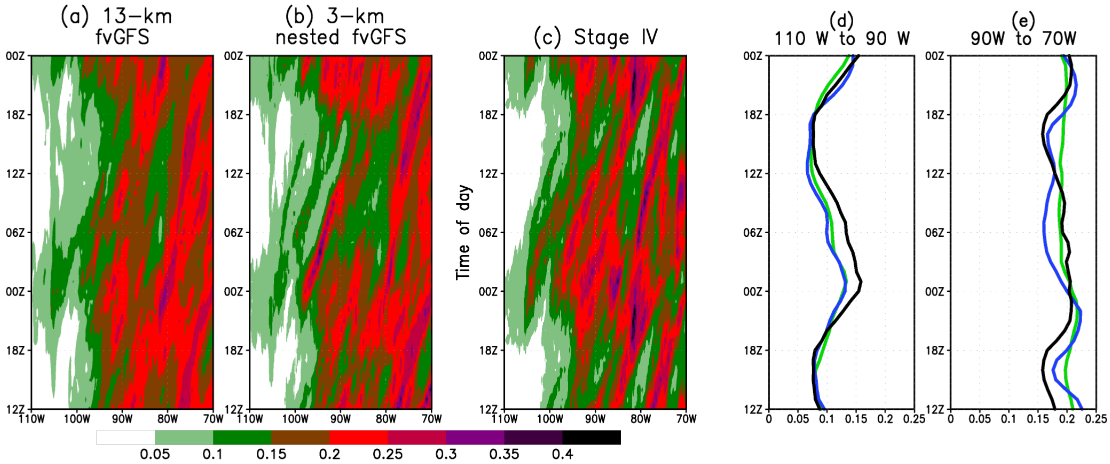

Figure 11. Time-longitude diagram of predicted hourly-accumulated precipitation (mm) averaged from 30 to 50 latitude and of forecasts for the period of 1–31 May 2017, showing lead times from 12 to 48 hours: (a) 13-km fvGFS; (b) nested fvGFS. (c) As in (a) and (b) but for observed Stage IV precipitation over the same time period, and showing one and a half cycles of the data. (d) Average precipitation (mm/hr) from 30 to 50 latitude and 110 to 90 west longitude, for 13-km (green) and nested fvGFS (blue) and Stage IV (black). (e) As in (d) but averaged from 90 to 70 west longitude.

rectly predicted from Missouri into Arkansas, and propagating eastward, up to five days in advance of the event. However, the squall lines propagate much more slowly the observed derechos or the predicted derechos in the nested fvGFS. While we expect that an environment favorable for derechos is predictable several days in advance, the 13-km fvGFS cannot be expected to represent the rapid propagation characteristic of derechos, owing to the lower resolution and the parameterized nature of the convection. This case demonstrates the potential of a global-to-regional model for multi-day *explicit* prediction of severe convective systems not possible with existing global prediction models.

5 Conclusion and prospects for a unified global-to-regional model

Regionally-refined global models show great promise for extending the convective-scale prediction capability of regional models from a single day to multiple days and to medium-range forecast scales, but present many scientific challenges not arising on regional scales. The nested global-to-regional version of fvGFS we have described for convective-scale prediction, through its stability, efficiency, and forecast skill, is capable of both excellent global-scale prediction, meeting or outperforming the operational GFS, while also showing the ability to explicitly predict individual convective storms up to five days in advance, and with precipitation skill comparable to operational convective-scale models. This explicit multi-day prediction would not be possible without skillful prediction of the global scales, which force and provide the predictability for the storm events, and the capacity for the model to represent marginally-resolved convective clouds. The fvGFS model is able to combine a skillful global prediction system and realistic simulation of storm-scale features into a single model, in the same forecast.

The introduction of a two-way nest into the global model does not disrupt the prediction skill of the large-scale circulation. The nested fvGFS shows only a minor reduction in the hemispheric 500-mb skill compared to the 13-km fvGFS, and after a short equilibration period still has a higher skill than the operational GFS, especially at longer lead times (5–7 days). The 3-km nest shows robust improvement in temperature and humidity biases compared to lower-

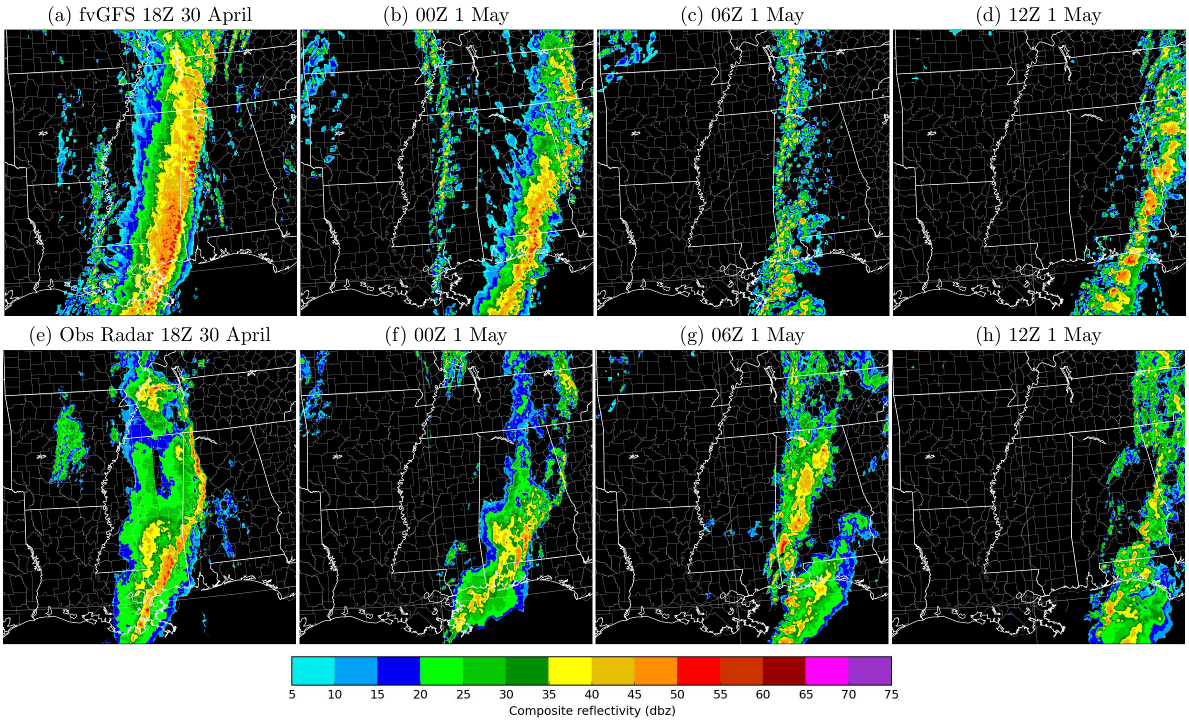

Figure 12. Composite reflectivity from fvGFS forecast initialized 00Z 30 April 2017 (top row, a–d) and observations (bottom row, e–h). Henceforth, all 3-km model output depicts shaded unsmoothed native nested-grid cells, unless otherwise stated.

resolution models, especially over the complex terrain of the western US. The 3-km nest also greatly improves precipitation biases, especially the low bias in extreme precipitation rates seen in the 13-km models, and is able to reproduce the propagation of individual convective systems. Precipitation skill in the nested fvGFS is competitive with the operational 3-km NAM nest, as are temperature and humidity biases in the Western US, although overall temperature and humidity errors are slightly higher.

Individual case evaluations focused on the depiction of warm-season severe weather events. Effective prediction of frontal squall lines, isolated single-cell and supercell storms, and of derechoes was demonstrated. These examples were used to illustrate some of the characteristics of fvGFS, including the simulated diurnal cycle and multi-day propagation of synoptic- and mesoscale precipitation systems, the spin-up from coarse-resolution initial conditions, the fine-scale structure of simulated storms (especially with respect to the representation of vorticity and updraft helicity) the source of multi-day predictability of favorable environments for severe convection, and the enhanced prediction value provided by refinement to convective scales.

The global-to-regional fvGFS configuration described in this paper has been tested and run on several NOAA supercomputing facilities. On Gaea-c4, using 1536 cores for the global grid and 1890 cores for the nested grid, the peak performance is about 18 min d^{-1}, or about twice the operational requirement of 8.5 min d^{-1}. A configuration of this unified global- and convective-scale model able to meet operational forecast needs is thereby well within the reach of current National Weather Service computing.

These results clearly show the promise of fvGFS for global-to-regional interactive modeling for improving predictions of severe weather events multiple days out, and the potential for prediction on seasonal-to-subseasonal prediction and for decadal-to-centennial climate pro-

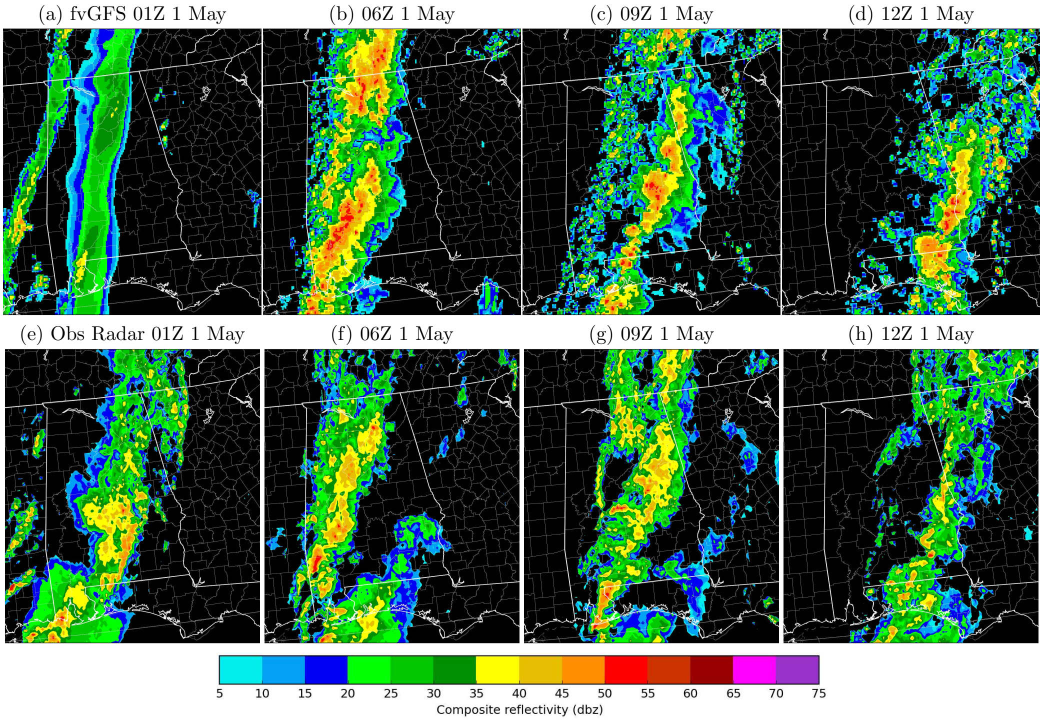

Figure 13. As in Figure 12, except (a–d) row is fvGFS forecasts initialized 01 May 2017. Note that (a) represents one hour after initialization, and so on.

jection. Further work at GFDL and with our university and agency partners is underway to improve fvGFS and similar models for prediction at all temporal and spatial scales, and to improve the physics, initialization, and the overall configuration for a wide range of forecast and research applications.

The results presented here make several strong points, potentially contrary to prevailing opinion. We have shown that an FV^3-based model can produce skillful forecasts and realistic simulation of convective-scale features. We have also shown that the GFS physics, when appropriately modified (especially with the introduction of a modern microphysical parameterization), is a powerful foundation for both convective-scale and global prediction. Finally, *we have shown that it is possible for a variable-resolution model to simultaneously produce skillful forecasts at every scale, from the hemispheric circulation down to convective scales*.

A: Nonhydrostatic nesting in FV^3

We describe here only the modifications to the procedure in Harris and Lin (2013).

The nested-grid boundary conditions for all prognostic variables, including nonhydrostatic vertical velocity and density, are linearly interpolated into the outermost halo (ghost) cells of the nested grid. Boundary conditions are updated every acoustic timestep by linearly interpolating from two earlier coarse-grid states; for positive-definite variables the extrapolation is limited so that the minimum value is non-negative. To compute the nonhydrostatic component of the pressure on the nested-grid boundary, the pressure is diagnosed using the same semi-implicit solver used in the interior for handling the fast-time scale vertically-propagating waves.

Two-way updating (nested-to-coarse communication) is always performed after the physics is called. The only fields that are updated to the coarse grid are the temperature, vertical ve-

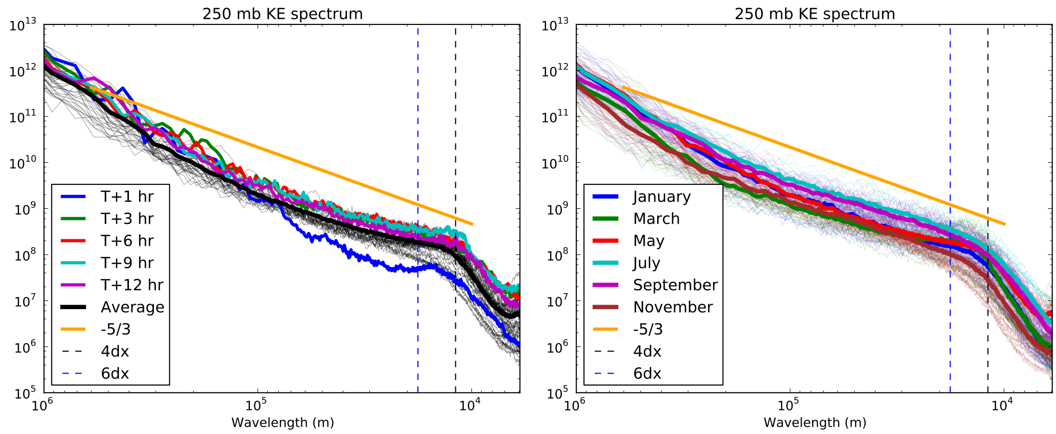

Figure 14. Nested-grid 250 mb kinetic energy spectra ($m^3\ s^{-2}$). Left: forecast initialized 01 May 2017. Light gray lines are plotted every three hours starting at 15Z on 01 May; the average of these times is shown as a heavy black line. Right: Time-averaged 250-mb kinetic energy spectra for six different forecasts at different times of the year.

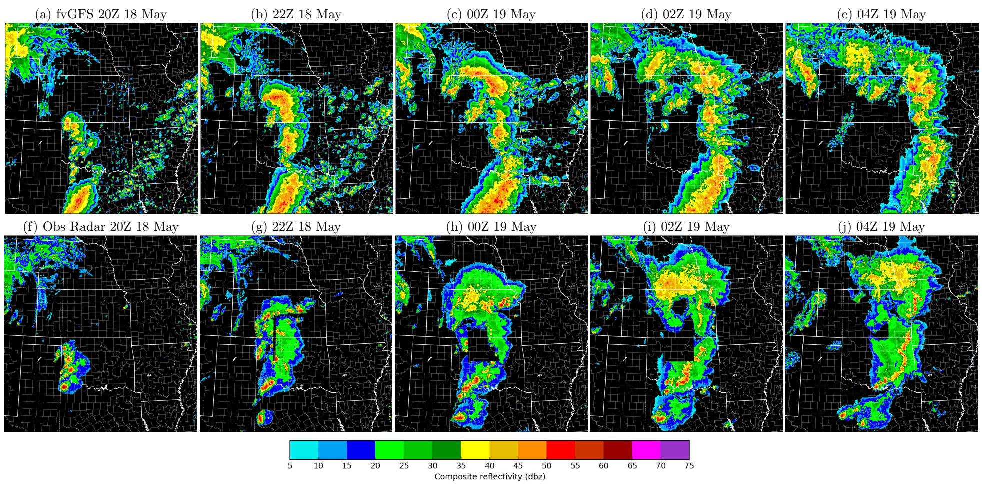

Figure 15. As in Figure 12 but for initialization at 00Z 18 May 2017.

locity, and staggered horizontal winds. Two-way updating of temperature and vertical velocity is done using the averaging procedure in Harris and Lin (2013), whereas the update of the horizontal winds uses the vorticity-conserving procedure described in the same paper.

Acknowledgments

Many individuals aided the development of fvGFS and FV^3. We would like to especially acknowledge Shian-Jiann Lin for leading the development of FV^3 core and the fvGFS model. We also thank Rusty Benson, Zhi Liang, Jan-Huey Chen, Xi Chen, and Kun Gao for their contributions to developing the fvGFS science and infrastructure. We thank JongIl Han for providing SA-SAS, George Gayno for his assistance with the land model and pre-processing tools, and Jacob Carley for providing processing tools for observed radar data. We thank Chuck Seman, Bill Hurlin, and especially Tim Supinie for their careful reviews of an earlier draft of the manuscript. We also thank Ming Xue, Eric Aligo, and the participants in the Hazardous Weather Testbed's Spring Forecasting Experiment for their feedback and advice. The partic-

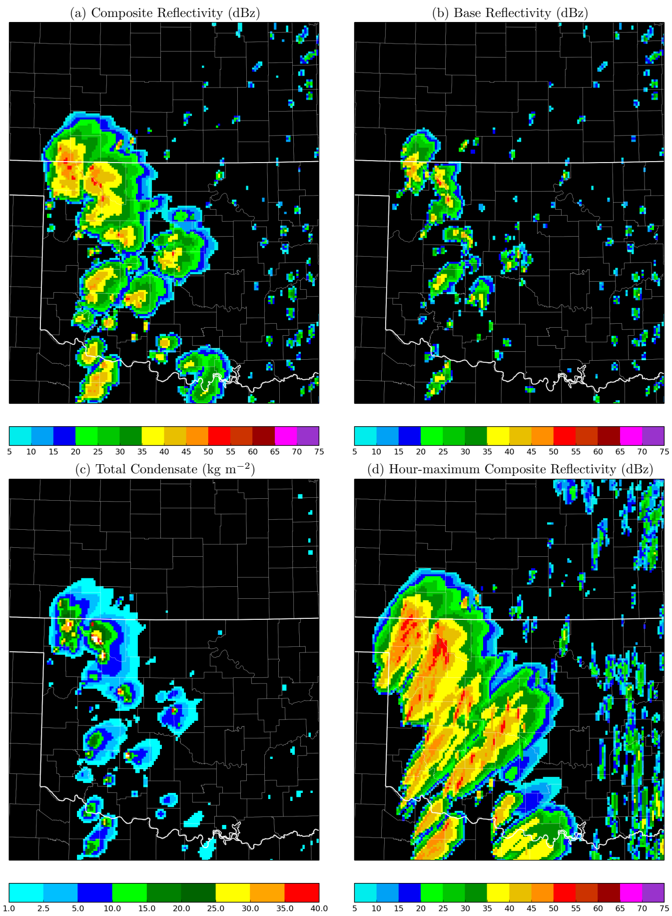

Figure 16. Nested fvGFS fields of a 20-hour forecast valid 20Z 18 May 2017. (a) Composite (column-maximum) reflectivity; (b) base (1-km above ground level) reflectivity; (c) Column integrated condensate; (d) Hourly-maximum composite reflectivity over the period 19Z to 20Z.

ipation of Morin, Rees, Zhou, and Stern was funded through the Next Generation Global Prediction System project from the NWS Office of Science and Technology Integration. All codes used for the simulations described in this paper are preserved in GFDL's GitLab version-control repository, and all data files for the simulations described in this paper are archived in the GFDL Tape Archive System; versions and data storage locations are described in the Supplemental Information.

References

Bauer, P., A. Thorpe, and G. Brunet (2015), The quiet revolution of numerical weather prediction, *Nature*, *525*(7567), 47–55.

Bey, I., D. Jacob, R. Yantosca, J. Logan, B. Field, A. Fiore, Q. Li, H. Liu, L. Mickley, M. Schultz, et al. (2001), Global modeling of tropospheric chemistry with assimilated meteorology- model description and evaluation, *J. Geophys. Res.*, *106*(23), 073–23.

Bogenschutz, P. A., A. Gettelman, C. Hannay, V. E. Larson, R. B. Neale, C. Craig, and C.-C. Chen (2017), The path to cam6: Coupled simulations with cam5.4 and cam5.5, *Geoscientific Model Development Discussions*, *2017*, 1–38, doi:10.5194/gmd-2017-129.

Chen, J.-H., and S.-J. Lin (2011), The remarkable predictability of inter-annual variability of Atlantic hurricanes during the past decade, *Geophys. Res. Lett.*, *38*(L11804), 6 pp.,

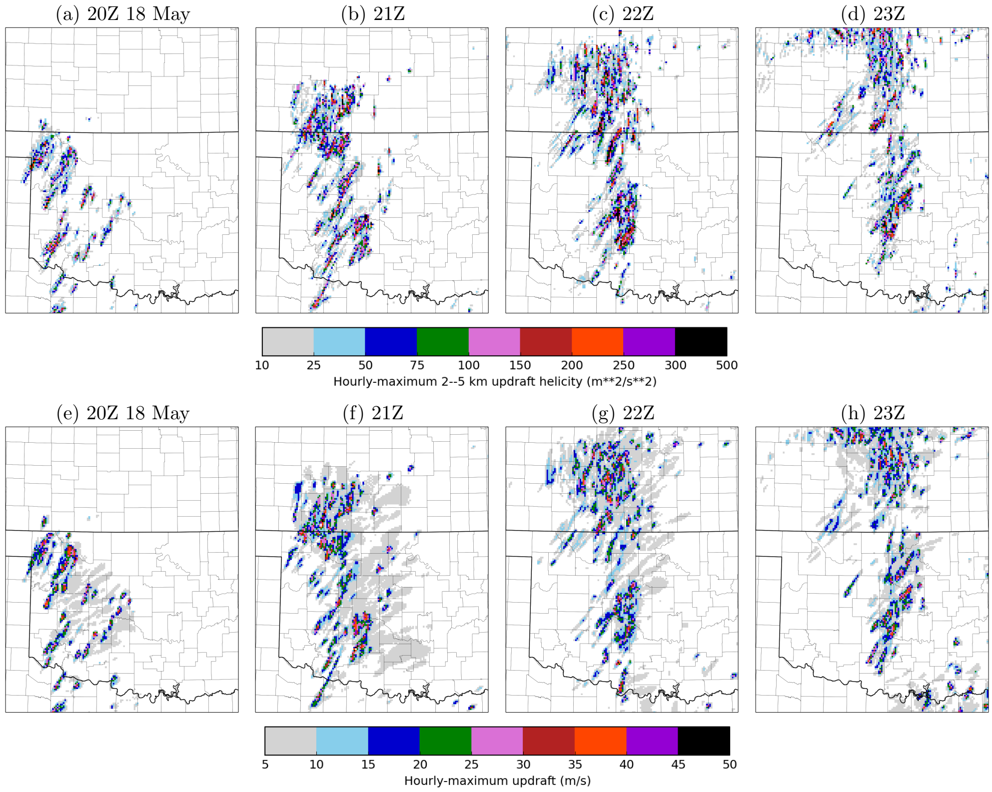

Figure 17. Nested fvGFS plots of hourly-maximum quantities of a forecast initialized 00Z 18 May 2017. (a–d): 2–5 km updraft helicity; (e–f): column-maximum updraft.

doi:10.1029/2011GL047629.

Chen, J.-H., and S.-J. Lin (2013), Seasonal Predictions of Tropical Cyclones Using a 25-km Resolution General Circulation Model, *J. Clim.*, *26*.

Chin, M., R. B. Rood, S.-J. Lin, J.-F. Müller, and A. M. Thompson (2000), Atmospheric sulfur cycle simulated in the global model gocart: Model description and global properties, *Journal of Geophysical Research: Atmospheres*, *105*(D20), 24,671–24,687.

Clark, P., N. Roberts, H. Lean, S. P. Ballard, and C. Charlton-Perez (2016), Convection-permitting models: a step-change in rainfall forecasting, *Meteorological Applications*, *23*(2), 165–181.

Clough, S., M. Shephard, E. Mlawer, J. Delamere, M. Iacono, K. Cady-Pereira, S. Boukabara, and P. Brown (2005), Atmospheric radiative transfer modeling: a summary of the aer codes, *Journal of Quantitative Spectroscopy and Radiative Transfer*, *91*(2), 233–244.

Corfidi, S. F., M. C. Coniglio, A. E. Cohen, and C. M. Mead (2016), A proposed revision to the definition of derecho, *Bulletin of the American Meteorological Society*, *97*(6), 935–949, doi:10.1175/BAMS-D-14-00254.1.

Delworth, T. L., A. J. Broccoli, A. Rosati, R. J. Stouffer, V. Balaji, J. A. Beesley, W. F. Cooke, K. W. Dixon, J. Dunne, K. Dunne, et al. (2006), Gfdl's cm2 global coupled climate models. part i: Formulation and simulation characteristics, *J. Clim.*, *19*(5), 643–674.

Denis, B., J. Côté, and R. Laprise (2002), Spectral decomposition of two-dimensional atmospheric fields on limited-area domains using the discrete cosine transform (dct), *Monthly Weather Review*, *130*(7), 1812–1829.

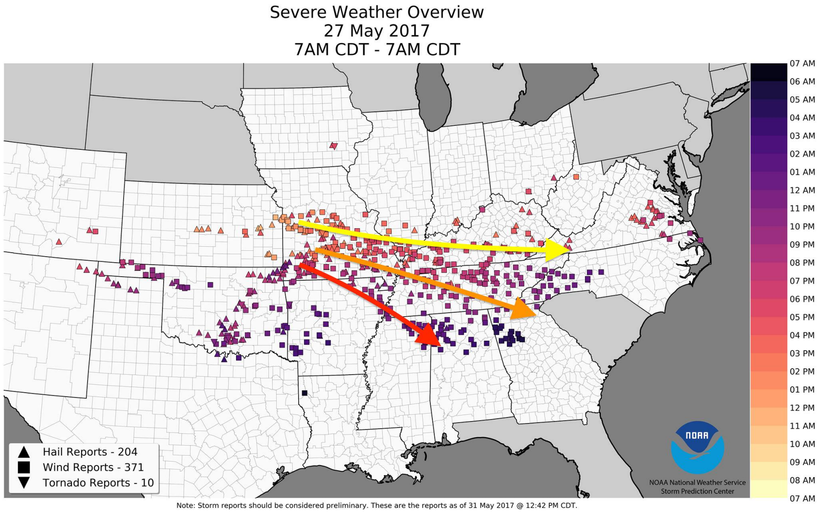

Figure 18. SPC preliminary storm reports for the 24 hours ending 12Z 28 May 2017, with subjectively-analyzed derecho tracks. (Plot courtesy SPC.)

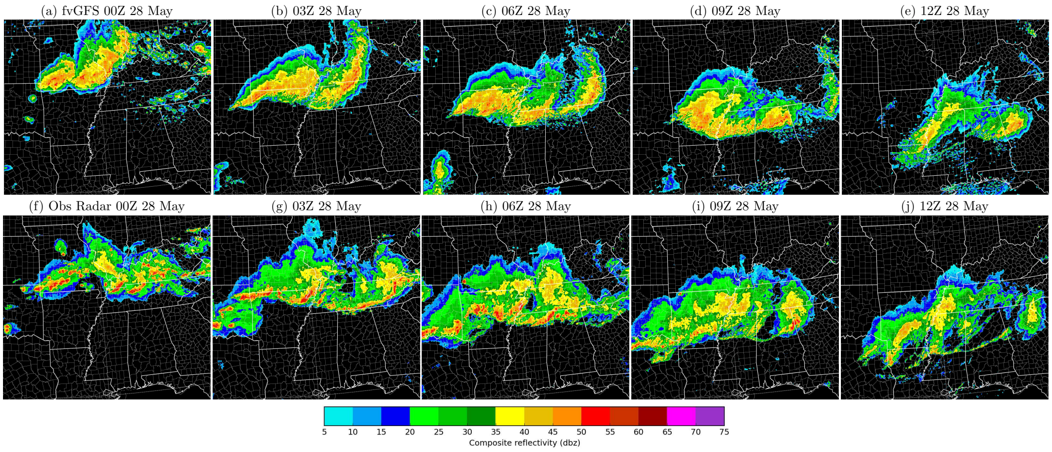

Figure 19. As in Figure 12, but for the forecast initialized 00Z 27 May 17.

Donner, L. J., B. L. Wyman, R. S. Hemler, L. W. Horowitz, Y. Ming, M. Zhao, J.-C. Golaz, P. Ginoux, S.-J. Lin, M. D. Schwarzkopf, et al. (2011), The dynamical core, physical parameterizations, and basic simulation characteristics of the atmospheric component AM3 of the GFDL global coupled model CM3, *J. Clim.*, *24*(13), 3484–3519.

Ek, M., K. Mitchell, Y. Lin, E. Rogers, P. Grunmann, V. Koren, G. Gayno, and J. Tarpley (2003), Implementation of noah land surface model advances in the national centers for environmental prediction operational mesoscale eta model, *Journal of Geophysical Research: Atmospheres*, *108*(D22).

Emanuel, K. A. (1989), Dynamical theories of tropical convection, *Australian Meteorological Magazine*, *37*(1).

Gelaro, R., W. McCarty, M. J. Suárez, R. Todling, A. Molod, L. Takacs, C. A. Randles, A. Darmenov, M. G. Bosilovich, R. Reichle, et al. (2017), The modern-era retrospective analysis for research and applications, version 2 (merra-2), *Journal of Climate*, *30*(14), 5419–5454.

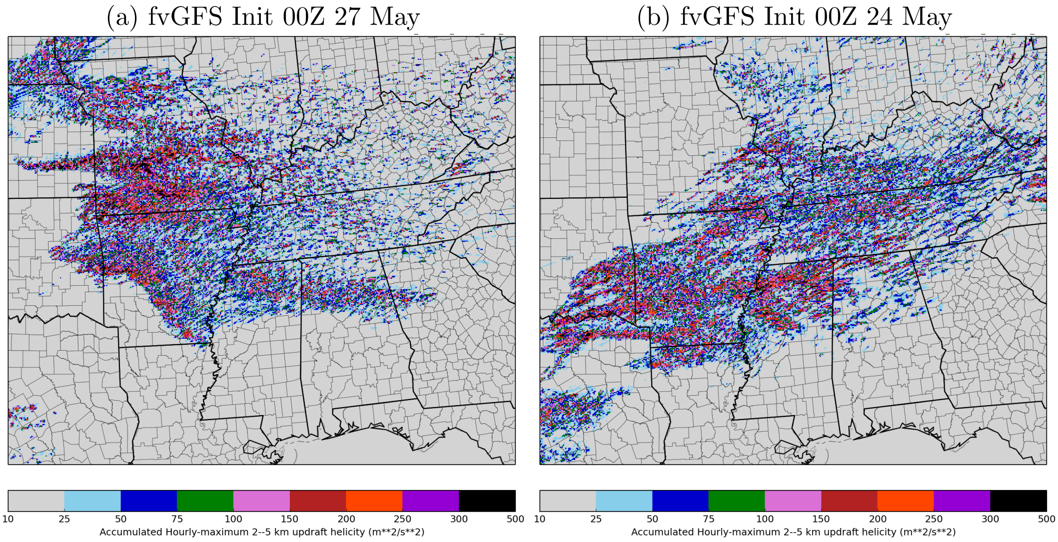

Figure 20. Maximum 2–5 km updraft helicity between 12Z on 27 May and 12Z on 28 May for fvGFS forecasts initialized (a) 00Z 27 May 17 and (b) 00Z 24 May 17.

Greybush, S. J., R. J. Wilson, R. N. Hoffman, M. J. Hoffman, T. Miyoshi, K. Ide, T. McConnochie, and E. Kalnay (2012), Ensemble kalman filter data assimilation of thermal emission spectrometer temperature retrievals into a mars gcm, *Journal of Geophysical Research: Planets*, *117*(E11).

Han, J., and H.-L. Pan (2011), Revision of convection and vertical diffusion schemes in the ncep global forecast system, *Weather and Forecasting*, *26*(4), 520–533.

Han, J., W. Wang, Y. C. Kwon, S.-Y. Hong, V. Tallapragada, and F. Yang (2017), Updates in the ncep gfs cumulus convection schemes with scale and aerosol awareness, *Weather and Forecasting*, (32).

Harris, L. M., and S.-J. Lin (2013), A Two-Way Nested Global-Regional Dynamical Core on the Cubed-Sphere Grid, *Mon. Wea. Rev.*, *141*(1), 283–306.

Harris, L. M., and S.-J. Lin (2014), Global-to-regional nested-grid climate simulations in the GFDL High Resolution Atmosphere Model, *J. Clim.*, *27*.

Harris, L. M., S.-J. Lin, and C. Tu (2016), High-resolution climate simulations using gfdl hiram with a stretched global grid, *Journal of Climate*, *29*(11), 4293–4314.

Hong, S.-Y., Y. Noh, and J. Dudhia (2006), A new vertical diffusion package with an explicit treatment of entrainment processes, *Monthly weather review*, *134*(9), 2318–2341.

Jeevanjee, N. (2017), Vertical velocity in the gray zone, *Journal of Advances in Modeling Earth Systems*.

Koshyk, J. N., B. A. Boville, K. Hamilton, E. Manzini, and K. Shibata (1999), Kinetic energy spectrum of horizontal motions in middle-atmosphere models, *Journal of Geophysical Research: Atmospheres*, *104*(D22), 27,177–27,190.

Lin, S. (1997), A finite-volume integration method for computing pressure gradient force in general vertical coordinates, *Q. J. Roy. Meteor. Soc.*, *123*, 1749–1762.

Lin, S., and R. Rood (1996), Multidimensional flux-form semi-Lagrangian transport schemes, *Mon. Wea. Rev.*, *124*, 2046–2070.

Lin, S.-J. (2004), A 'vertically Lagrangian' finite-volume dynamical core for global models, *Mon. Wea. Rev.*, *132*, 2293–2307.

Lin, S.-J., and R. Rood (1997), An explicit flux-form semi-Lagrangian shallow-water model on the sphere., *Q.J.R.Meteorol.Soc.*, *123*, 2477–2498.

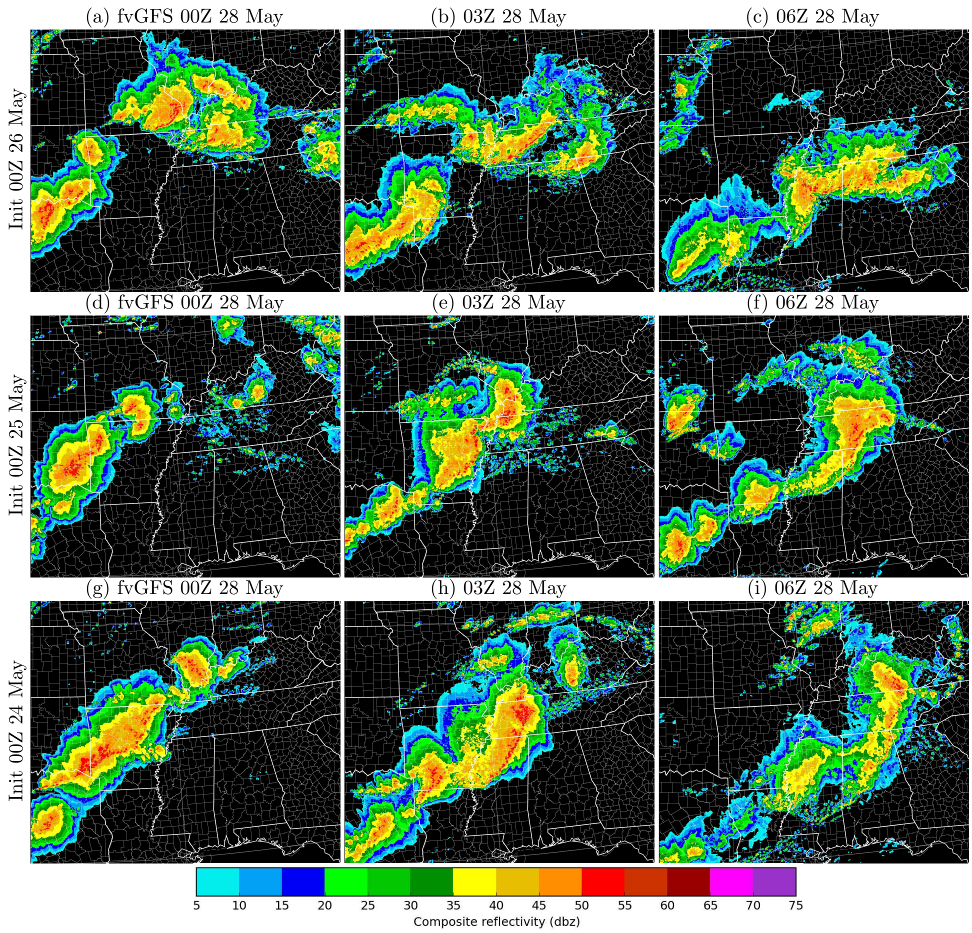

Figure 21. Multi-day forecasts of the 27 May event. (a–c): initialization 00Z 26 May. (d–f): initialization 00Z 25 May. (g–i): initialization 00Z 24 May.

Lin, S.-J., L. M. Harris, R. Benson, L. Zhou, J.-H. Chen, and X. Chen (2017), Towards a Unified Prediction System from Weather to Climate Scale, in *Second Symposium on Multi-Scale Atmospheric Predictability, Seattle, WA*, Paper 3.1.

Lin, Y. (2011), Gcip/eop surface: Precipitation ncep/emc 4km gridded data (grib) stage iv data, version 1.0.

Lin, Y., and K. E. Mitchell (2005), 1.2 the ncep stage ii/iv hourly precipitation analyses: Development and applications, in *19th Conf. Hydrology, American Meteorological Society, San Diego, CA, USA*.

Murakami, H., G. A. Vecchi, S. Underwood, T. L. Delworth, A. T. Wittenberg, W. G. Anderson, J.-H. Chen, R. G. Gudgel, L. M. Harris, S.-J. Lin, et al. (2015), Simulation and prediction of category 4 and 5 hurricanes in the high-resolution gfdl hiflor coupled climate model, *Journal of Climate*, *28*(23), 9058–9079.

Murphy, A. H., and E. S. Epstein (1989), Skill scores and correlation coefficients in model verification, *Monthly weather review*, *117*(3), 572–582.

Nastrom, G., and K. S. Gage (1985), A climatology of atmospheric wavenumber spectra of wind and temperature observed by commercial aircraft, *Journal of the atmospheric sciences*, *42*(9), 950–960.

Neale, R. B., C.-C. Chen, A. Gettelman, P. H. Lauritzen, S. Park, D. L. Williamson, A. J. Conley, R. Garcia, D. Kinnison, J.-F. Lamarque, et al. (2010), Description of the ncar

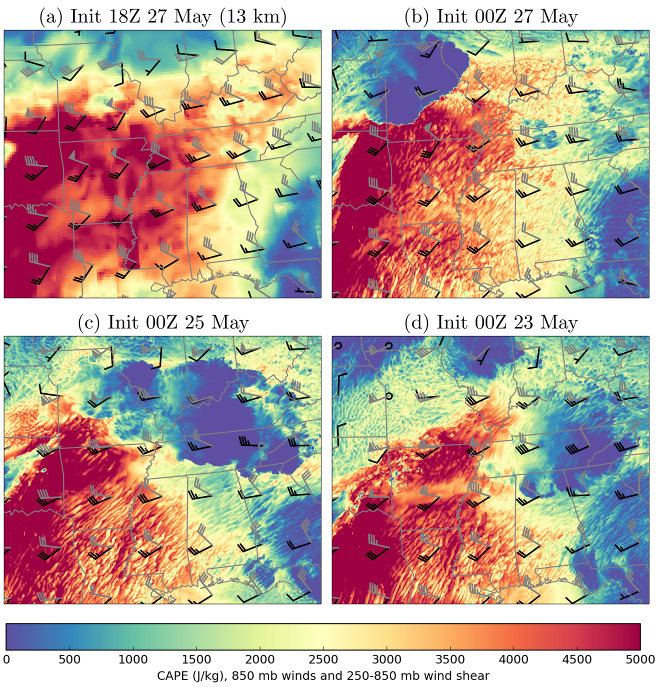

Figure 22. Convective available potential energy (shading), 850-mb winds (black wind barbs) and 250-mb to 850-mb wind shear (gray) valid 21Z 27 May 2017: (a) 13-km fvGFS initialized 18Z on 27 May 2017, a surrogate "analysis" (b–d) nested fvGFS forecasts initialized (b) one day (c) three days and (d) five days prior to the event.

community atmosphere model (cam 5.0), *NCAR Tech. Note NCAR/TN-486+ STR*.

Putman, W. M., and S.-J. Lin (2007), Finite-volume transport on various cubed-sphere grids, *J. Comput. Phys.*, *227*(1), 55–78.

Putman, W. M., and M. Suarez (2011), Cloud-system resolving simulations with the NASA Goddard Earth Observing System global atmospheric model (GEOS-5), *Geophysical Research Letters*, *38*(16).

Rienecker, M. M., M. J. Suarez, R. Gelaro, R. Todling, J. Bacmeister, E. Liu, M. G. Bosilovich, S. D. Schubert, L. Takacs, G.-K. Kim, et al. (2011), MERRA: NASA's modern-era retrospective analysis for research and applications,, *Journal of climate*, *24*(14), 3624–3648.

Roberts, N. M., and H. W. Lean (2008), Scale-selective verification of rainfall accumulations from high-resolution forecasts of convective events, *Monthly Weather Review*, *136*(1), 78–97.

Schmidt, F. (1977), Variable fine mesh in spectral global models, *Beitr. Phys. Atmos.*, *50*, 211–217.

Shen, B.-W., R. Atlas, J.-D. Chern, O. Reale, S.-J. Lin, T. Lee, and J. Chang (2006), The 0.125 degree finite-volume general circulation model on the nasa columbia supercomputer: Preliminary simulations of mesoscale vortices, *Geophysical Research Letters*, *33*(5).

Suarez, M. J., M. Rienecker, R. Todling, J. Bacmeister, L. Takacs, H. Liu, W. Gu, M. Sienkiewicz, R. Koster, R. Gelaro, et al. (2008), The geos-5 data assimilation system-documentation of versions 5.0. 1, 5.1. 0, and 5.2. 0.

Thompson, G., P. R. Field, R. M. Rasmussen, and W. D. Hall (2008), Explicit forecasts of winter precipitation using an improved bulk microphysics scheme. part ii: Implementation of a new snow parameterization, *Monthly Weather Review*, *136*(12), 5095–5115.

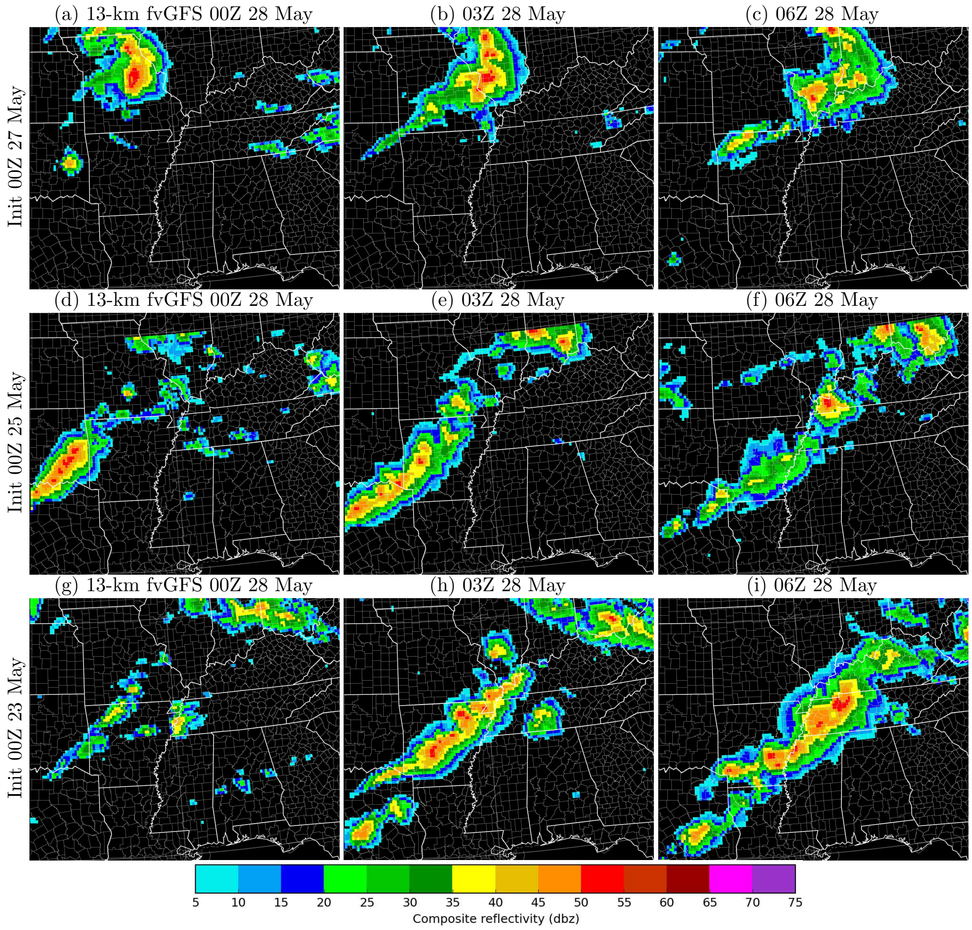

Figure 23. As in Figure 21, but for the 13-km fvGFS and for initializations of (a–c) 00Z 27 May, (d–f) 00Z 25 May, and (g–i) 00Z 23 May.

Walters, D., I. Boutle, M. Brooks, M. Thomas, R. Stratton, S. Vosper, H. Wells, K. Williams, N. Wood, T. Allen, et al. (2017), The met office unified model global atmosphere 6.0/6.1 and jules global land 6.0/6.1 configurations, *Geoscientific Model Development*, *10*(4), 1487.

Wang, C.-C. (2014), On the calculation and correction of equitable threat score for model quantitative precipitation forecasts for small verification areas: The example of taiwan, *Weather and Forecasting*, *29*(4), 788–798, doi:10.1175/WAF-D-13-00087.1.

Wei, H., W. Zheng, J. Meng, G. Gayno, Y. Hou, and M. Ek (2017), Planned land surface changes for the next nems implementation, in *28th Conf. on Weather Analysis and Forecasting/ 24th Conf. on Numerical Weather Prediction, American Meteorological Society, Seattle, WA*, 600.

Xu, K.-M., and D. A. Randall (1996), A semiempirical cloudiness parameterization for use in climate models, *Journal of the atmospheric sciences*, *53*(21), 3084–3102.

Zhao, M., I. M. Held, S.-J. Lin, and G. A. Vecchi (2009), Simulations of Global Hurricane Climatology, Interannual Variability, and Response to Global Warming Using a 50-km Resolution GCM, *J. Clim.*, *22*(24), 6653–6678, doi:10.1175/2009JCLI3049.1.

Zhao, M., J.-C. Golaz, I. Held, V. Ramaswamy, S.-J. Lin, Y. Ming, P. Ginoux, B. Wyman, L. Donner, D. Paynter, et al. (2016), Uncertainty in model climate sensitivity traced to representations of cumulus precipitation microphysics, *Journal of Climate*, *29*(2),

543–560.
Zhao, Q., and F. H. Carr (1997), A prognostic cloud scheme for operational nwp models, *Monthly Weather Review*, *125*(8), 1931–1953.